



1 **A free, open-source method for automated mapping of quantitative mineralogy from energy-dispersive X-**
2 **ray spectroscopy scans of rock thin sections**

3 Miles M. Reed¹, Ken L. Ferrier¹, William O. Nachlas¹, Bil Schneider¹, Chloé Arson², Tingting Xu³, Xianda
4 Shen^{4,5}, and Nicole West⁶

5 ¹ Geoscience, University of Wisconsin-Madison, United States

6 ² Civil and Environmental Engineering, Cornell University, United States

7 ³ Hopkins Extreme Materials Institute, John Hopkins University, United States

8 ⁴ Key Laboratory of Geotechnical and Underground Engineering of Ministry of Education, Tongji University,
9 China

10 ⁵ Department of Geotechnical Engineering, Tongji University, China

11 ⁶ Independent Researcher

12 *Correspondence to:* Miles Reed (miles.reed@wisc.edu)

13 **Abstract**

14 Quantitative mapping of minerals in rock thin sections delivers data on mineral abundance, size, and spatial
15 arrangement that are useful for many geoscience and engineering disciplines. Although automated methods for
16 mapping mineralogy exist, these are often expensive, associated with proprietary software, or require
17 programming skills, which limits their usage. Here we present a free, open-source method for automated
18 mineralogy mapping from energy dispersive spectroscopy (EDS) scans of rock thin sections. This method uses a
19 random forest machine learning image classification algorithm within the QGIS geographic information system
20 and Orfeo Toolbox, which are both free and open source. To demonstrate the utility of this method, we apply it to
21 14 rock thin sections from the well-studied Rio Blanco tonalite lithology of Puerto Rico. Measurements of
22 mineral abundance inferred from our method compare favourably to previous measurements of mineral
23 abundance inferred from X-ray diffraction and point counts on thin sections. The model-generated mineral maps
24 agree with independent, manually-delineated mineral maps at a mean rate of 95%, with accuracies as high as
25 96% for the most abundant phase (plagioclase) and as low as 72% for the least abundant phase (apatite) in these
26 samples. We show that the default random forest hyperparameters in Orfeo Toolbox yielded high accuracy in the
27 model-generated mineral maps, and we demonstrate how users can determine the sensitivity of the mineral maps
28 to hyperparameter values and input features. These results show that this method can be used to generate accurate
29 maps of major mineral phases in rock thin sections using entirely free and open-source applications.

30

31 **1 Introduction**



32 Minerals are the fundamental units of rocks and many engineered materials (Perkins, 2020; Callister and
33 Rethwisch, 2020). Improving the quantification of mineral properties is a longstanding research objective in
34 industry and academic research (Pirrie and Rollinson, 2011), given the importance of mineral properties in
35 chemical weathering (e.g., Hilton and West, 2020), rock damage (e.g., Shen et al., 2019; Xu et al., 2022),
36 planetary evolution (e.g., Hazen et al., 2008), crustal deformation (e.g., Burgmann and Dresen, 2008), and
37 nutrient supply (e.g., Callahan et al., 2022). Quantitative mineralogy, the mapping of mineral phases across a
38 sample, results in measurements of mineral modal abundance, mineral grain size and shape, and the spatial
39 arrangement of minerals amongst one another (Schulz et al., 2020). Modal abundance is useful because it can
40 yield information on the sedimentary and tectonic environments in which the rock formed (Harlov et al., 1998;
41 Hupp and Donovan, 2018), while the spatial arrangement of minerals in a rock, termed rock fabric, can yield
42 further data on mechanical anisotropy and paleo-environmental conditions during the rock's formation and
43 metamorphism (Přikryl, 2006; Bjørlykke, 2014). Simultaneous quantification of modal mineralogy and detailed
44 mapping of the spatial arrangement of minerals in an automated manner, or automated mineralogy, is thus a key
45 tool for investigating many geologic processes. Wide adoption of automated mineralogy techniques are limited
46 by the prohibitive cost or programming skills required to use many automated mineralogy software applications,
47 so this technique has been mostly restricted to ore characterization, resource processing, and petroleum geology
48 (Nikonow and Rammlmair, 2017; Schulz et al., 2020).

49

50 In practice, automated mineralogy methods use a combination of image analysis and classification methods to
51 identify mineral phases from elemental composition data (or their derivatives), which can be collected with a
52 variety of analytical methods, including energy dispersive X-ray spectroscopy (EDS), wavelength dispersive X-
53 ray spectrometry (WDS), micro-X-ray fluorescence (μ -XRF), and laser-ablation inductively-coupled mass
54 spectroscopy (LA-ICP-MS) (Nikonow et al., 2019). Automated mineralogy is being slowly adopted by
55 researchers outside of resource extraction for combined modal analysis of bulk mineralogy, estimates of grain
56 size distribution, and mineral association (Han et al., 2022), which can be useful in a variety of disciplines such
57 as petrology, applied geochemistry, and rock mechanics (Sajid et al., 2016; Elghali et al., 2018; Rafiei et al.,
58 2020).

59

60 Automated mineralogy from EDS with the aid of back-scattered electron (BSE) imaging has been developing
61 since the 1980s and has grown alongside advances in scanning electron microscopy (SEM) and image processing
62 algorithms (Miller et al., 1983; Fandrich et al., 2007). Commercial automated mineralogy systems are available



63 as integrated hardware-software systems or as standalone software packages which are combined with scanning
64 electron microscopes (Schulz et al., 2020). Some systems only work with certain scanning electron microscopes
65 and detectors from the same company QEMSCAN (Gottlieb et al., 2000), FEI-MLA (Fandrich et al., 2007), and
66 TESCAN TIMA-X (Hrstka et al., 2018). Others are purely software-based solutions which are integrated with
67 various SEMs: ZEISS Mineralogic, Oxford AZTecMineral, and Thermo-Scientific MAPS Mineralogy. The price
68 of hardware and software upgrades required to accommodate these systems renders them cost prohibitive to
69 many labs outside the resource extraction industry (Nikonow and Rammlmair, 2017). All systems have some
70 general ability to classify EDS spectra based on a database of pre-defined and/or customizable mineral spectra
71 standards (Schulz et al., 2020). Since the underlying software is proprietary, no source code is available for these
72 systems, and details on how they use spectra to classify mineral phases are sparse to non-existent (Kuelen et al.,
73 2020). Furthermore, the accuracy of mineral phase prediction from these systems has rarely been quantified
74 (Blannin et al., 2021).

75

76 To date, several open-source (i.e., source code is available and modifiable) automated mineralogy solutions have
77 been implemented. Ortolano et al. (2014, 2018) predicted mineralogy from a multistep workflow involving
78 principal component analysis, maximum likelihood classification, and multi-linear regression performed on EDS
79 or WDS spectral data using the Python extension within ArcGIS. Li et al. (2021) used a variety of legacy
80 machine-learning and deep-learning models to classify minerals in oil reservoir rocks using mineral maps
81 generated from proprietary software as training data. In terms of image classification, deep-learning methods are
82 state of the art but currently require the user to be relatively adept at programming and knowledgeable of the
83 computer vision principles employed (Khan et al., 2018; Zhang et al., 2019). A method that requires little to no
84 programming ability would allow more users to benefit from automated mineralogy data. An example of this
85 approach is XMapTools by Lanari et al. (2014), a graphical, open-source automated mineralogy solution with
86 multiple machine-learning classification algorithms within a standalone, MATLAB-based environment.

87

88 The main goal of this study is to present a new, user-friendly quantitative automated mineralogy method that we
89 developed and implemented within QGIS, a free and open-source geographic information system. Nikonow and
90 Rammlmair (2017) previously showed success in adapting the proprietary remote-sensing package ENVI to do
91 automated mineralogy using μ -XRF data. Here, we use the free and open-source Orfeo Toolbox plugin for QGIS
92 (Grizonnet et al., 2017) to predict thin-section scale bulk mineralogy from EDS elemental intensity data using a
93 random forest (RF) image classifier (Breiman, 2001). Random forest classification is a supervised classification



94 algorithm (i.e., the user generates training data) in which an ensemble of decision trees produces a majority vote
95 that assigns a thematic classification to unknown data (Breiman, 2001). Each decision tree within the ensemble is
96 trained on a random sampling of the training data using only a set number of random features at each branch
97 (Cutler et al., 2011). During prediction, for each decision tree, unknown data traverses a sequence of rule-based
98 branches which culminate in the assignation of a predicted class (Breiman, 2001). Each tree gets one vote for
99 each pixel; the predicted class with the most votes is assigned to the unknown data. There are several reasons
100 why RF classification is useful for automated mineralogy mapping. It is well suited for accommodating
101 unbalanced training data and nonparametric data distributions (Maxwell et al., 2018), which are common in rock
102 samples due to large differences in relative mineral abundances and elemental intensities (Ahrens, 1954). In
103 addition, recent work showed that RF classification performed better than other legacy machine-learning
104 algorithms (e.g., support-vector machines; Hearst et al., 1998) in mineral classification of reservoir rocks (Li et
105 al., 2021).

106

107 Unlike previous methods, the method presented here uses only freely available and open-source applications, and
108 it requires no programming on the part of the user. Situating the workflow within a GIS environment has
109 advantages over standalone programs such as direct access to raster and vector manipulation and analysis tools
110 and database management (Tarquini and Favalli, 2010; Berrezueta et al., 2019). In the remainder of this study, we
111 present an overview of the automated mineralogy method and apply it to a set of rock samples from the Rio
112 Blanco tonalite to demonstrate the method's utility. By outlining an easy-to-use and open-source solution, we
113 hope this method provides a tool for automated mineralogy to a broader community of users.

114

115 **2 Overview of the method**

116

117 The goal of our automated mineralogy method is to produce quantitative mineralogy maps of rock thin sections
118 solely from EDS data. Here in Section 2, we briefly summarize each step needed to reach a predicted mineral
119 map. In Section 3, we demonstrate how to use the method by applying it to a set of rock thin sections, during
120 which we elaborate on the choices users need to make and the functions they need to use during each step. We
121 also provide a detailed step-by-step guide in the supplementary information (Reed et al., 2024).

122

123 The starting point for this method is EDS-generated scans of rock thin sections. For the purposes of our method,
124 we take these scans as already measured and in hand. Generating such scans requires preparing thin sections and



125 analyzing them with a scanning electron microscope, both of which are done by established procedures
126 (Goldstein et al., 2018). The necessary output from such scans are rasters of elemental intensity (counts/eV), one
127 for each element of interest (e.g., Ca, Na, K, etc.). After the EDS elemental intensity rasters have been generated,
128 all the remaining steps in the method are conducted in QGIS. No programming is required in any step. Instead,
129 users need only be familiar with QGIS and their samples.

130
131 The first step is to ensure all the necessary information is in place. This involves importing the raw elemental
132 intensity rasters into QGIS with no coordinate reference system (Fig. 1a). This also involves compiling a list of
133 all the mineral phases that will be mapped in the thin section, which can be assessed based on prior knowledge,
134 literature, and examination of EDS spectra. As we describe in Section 4, we recommend restricting this to
135 mineral phases with sufficiently high abundance to be accurately mapped.

136
137 The second step is to smooth the raw elemental intensity rasters (Fig. 1b). This is useful because EDS-generated
138 elemental intensity rasters are subject to noise, which can arise through electron beam interactions with the
139 sample and incorrect spectral peak identification by the EDS software (Goldstein et al., 2018). As we describe in
140 Section 4.3, we found that this smoothing step was best done with a 7-pixel radius circular mean filter. Here, a
141 mean filter is an image processing operation where a circular sliding window with a fixed radius surrounding a
142 center pixel moves across an input raster one pixel at a time and, in an output raster, assigns a mean value to the
143 center pixel based on the surrounding pixels (Gonzalez and Woods, 2017). We performed this on intensity rasters
144 from the example samples we applied our method to in Section 3. For this, we used the free and open-source
145 System for Automated Geoscientific Analyses (SAGA) plugin for QGIS (Conrad et al., 2015).

146
147 The third step is to gather the smoothed elemental intensity rasters into a virtual raster with one band for each
148 element of interest (Fig. 1c). For example, if the user chooses to import elemental intensity rasters for six
149 elements, as we did in the application of this method to our samples in Section 3, this will result in a virtual raster
150 with six bands. For this, we used the Geospatial Data Abstraction Library (GDAL/OGR contributors, 2022),
151 which is a standard library in QGIS.

152
153 The fourth step is to train a RF image classification model on the virtual raster (Fig. 1d). This requires generating
154 a large number (~hundreds) of small polygons on the virtual raster. Each of these small polygons must lie within
155 a single mineral phase, which the user must identify and assign to the polygon. Collectively, these small polygons



156 must cover all the mineral phases of interest in the thin section in sufficient number to train the RF model. If the
157 user wishes to assess the accuracy of the RF-predicted mineral map to a manually mapped portion of the thin
158 section after the method is complete, we recommend restricting the location of these small training polygons to a
159 relatively small portion of the thin section (~10-20%). This will ensure that other portions of the thin section can
160 be mapped manually to compare against the RF-predicted mineral map. If the user does not wish to conduct such
161 an accuracy assessment after the RF-predicted mineral map is complete, then these small training polygons can
162 be generated anywhere across the entire thin section.

163

164 After the RF model has been trained, the fifth step is to apply the trained RF model to the entire virtual raster
165 (Fig. 1e). During this step, the RF model assigns a mineral phase to every pixel in the virtual raster, which yields
166 a mineral map for the entire thin section. For these RF modeling steps, we used the free, open-source Orfeo
167 Toolbox plugin for QGIS (Grizonnet et al., 2017).

168

169 The sixth and final step is to denoise the RF-generated mineral map (Fig. 1f). For this, we applied a circular
170 majority filter using the SAGA plugin for QGIS. A majority filter is akin to the mean filter described above but
171 assigns the modal value of the surrounding pixels to the pixel in the output raster at the center sliding window
172 (Gonzalez and Woods, 2017). As we describe in Section 4.3, we found that this was best done with a 10-pixel
173 radius majority filter in the example samples we applied this to in Section 3. This eliminates most isolated pixels
174 within larger groups of pixels of a uniform predicted mineral phase and rare pixels that were not classified due to
175 voting ties (Ortolano et al., 2018; Nikonow et al., 2019)

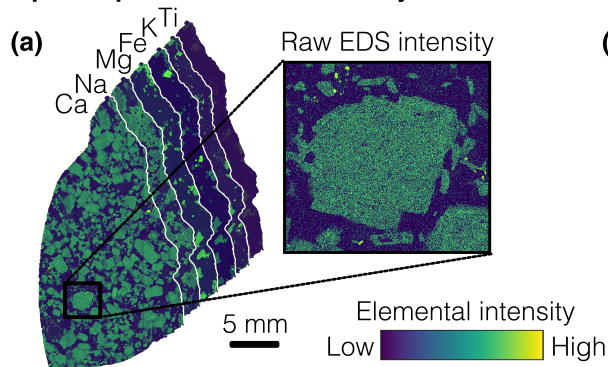
176

177 At this stage, the RF-predicted mineral map is complete. It can now be interrogated or manipulated according to
178 the user's needs. For instance, the mineral map can be converted from a raster to a vector form to facilitate
179 measurement of mineral grain size and other properties (Section 5.2).

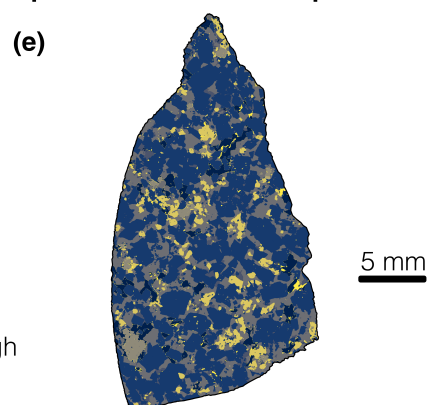
180



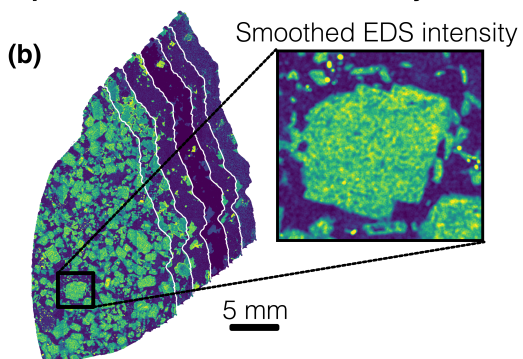
Step 1: Import elemental intensity rasters



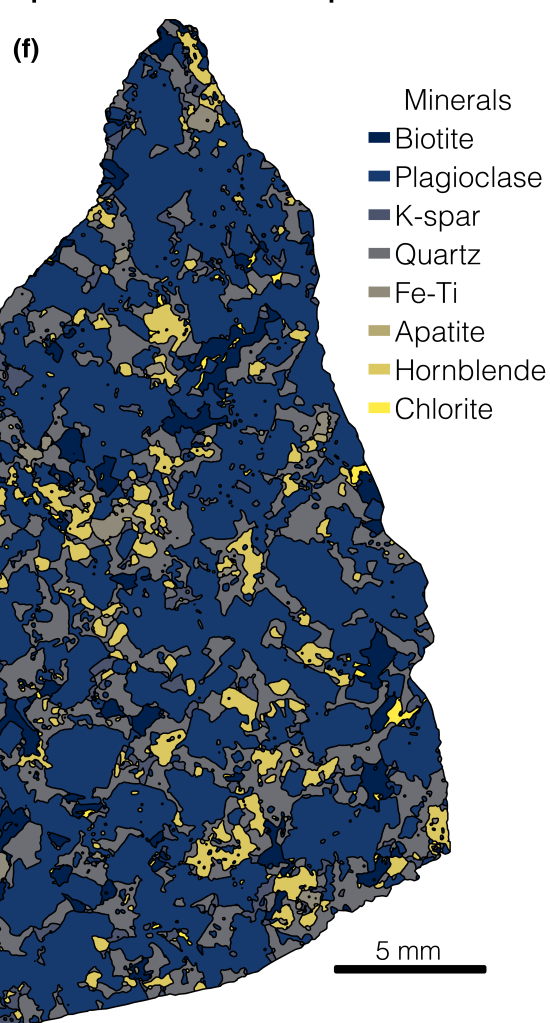
Step 5: Create mineral map



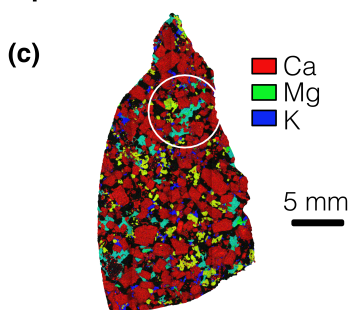
Step 2: Smooth elemental intensity rasters



Step 6: Smooth mineral map



Step 3: Create virtual raster



Step 4: Train random forest model

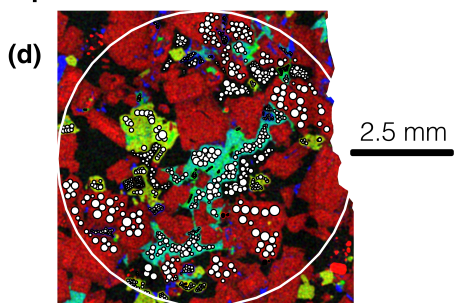




Figure 1. Example application of the automated mineralogy method. (a) Step 1: Import raw elemental intensity rasters (Ca, Na, Mg, Fe, K and Ti) into QGIS. Here, the rasters shown are for the thin-section sample 1-13a. The zoomed-in view of the Ca raster exemplifies the short-wavelength noise in the elemental rasters. (b) Step 2: Smooth each elemental intensity raster with a circular mean filter. The zoomed-in view shows that this filter has eliminated much of the short-wavelength noise that was in the raw elemental rasters. (c) Step 3: Create a virtual raster by combining the smoothed elemental rasters into a single image container with bands for each element. The white circle shows the area within which polygons were generated to train the random forest (RF) model in Step 4. (d) Step 4: Within the training area boundary in the virtual raster (large white circle, as in Step 3), draw a series of small polygons (here, small white circles). Each polygon must lie within a single known mineral phase, and collectively these small polygons must sample all mineral phases of interest (here, plagioclase feldspar, quartz, hornblende, biotite, potassium feldspar, Fe-Ti oxides, apatite, and chlorite). These polygons collect the pixel-level data on which the RF model will be trained. (e) Step 5: Apply the trained RF model to the entire sample to create a thin section-scale mineral map. (f) Step 6: Smooth the RF-predicted mineral map with a circular majority filter.

181

182

183 **3 Application of the method**

184

185 **3.1 Preparation of rock thin sections from the Luquillo Critical Zone Observatory**

186 To demonstrate the utility of the method described in Section 2, we applied it to 14 thin sections of Rio Blanco
187 tonalite from the Luquillo Critical Zone Observatory (LCZO) in Puerto Rico, United States, a site that has been
188 the subject of substantial research on the weathering of igneous rocks into saprolite and soil (White et al., 1998;
189 Riebe et al., 2003; Stallard and Murphy, 2012; Brocard et al., 2023). The lithology is a phaneritic, plutonic
190 igneous rock with some evidence of low-grade hydrothermal alteration (Speer, 1984). The Rio Blanco tonalite
191 provides an ideal case study because mineral abundance has been characterized previously via quantitative X-ray
192 diffraction (XRD) and point counting modal analysis (i.e., systematic manual identification and counting under
193 microscope; Ingersoll et al., 1984), which indicated the rock consists of plagioclase feldspar (andesine), quartz,
194 biotite, hornblende, potassium feldspar, magnetite, apatite, and chlorite (Murphy et al., 1998; Buss et al., 2008;
195 Ferrier et al., 2010).



196

197 To ready the samples for EDS, 14 petrographic thin sections were prepared on 27 x 46 mm glass slides from
198 bedrock core quarters collected from the Rio Icaos catchment within the LCZO (Comas et al., 2019). The
199 samples ranged in area from 34.7 to 139.5 mm². Four samples are composed of weathered rock nearer to the
200 surface while the rest are more pristine bedrock (Orlando et al., 2016). From each core depth, two thin sections
201 were prepared in vertical and horizontal orientations. Our own preliminary optical microscopy observations
202 revealed that these samples contained abundant plagioclase, quartz, hornblende, and biotite, which is consistent
203 with previous modal analyses (Murphy et al., 1998; Buss et al., 2008).

204

205 **3.2 Measuring elemental intensity in thin sections with energy dispersive spectroscopy**

206 Each thin section was mapped with energy dispersive X-ray spectroscopy (EDS) using a Hitachi S-3400 VP-
207 SEM with a thermionic tungsten electron source equipped with an Oxford Instruments X-Act 10 mm² silicon drift
208 detector receiving X-rays across 2048 spectral bands. The EDS detector acquires a spectrum showing the energy
209 and intensity of characteristic X-rays emitted from the sample to determine the atomic composition of the sample
210 within the analysis volume of the primary beam (Goldstein et al., 2018). For our measurements on our thin
211 sections, the beam step size and magnification resulted in full thin-section elemental intensity maps (counts/eV)
212 at a resolution of 4 μm/pixel. EDS data were acquired with accelerating voltage of 15 kV and beam current of
213 ~10 nA. Dwell time per beam step, which governs the amount of time the detector counts X-rays, was 200 ms
214 (Newberry and Ritchie, 2013a). EDS acquisition time was ~3.5 hours for each thin section.

215

216 From the EDS analysis application included with this instrument (AZtec), we exported six TIF files for each
217 sample (Fig. 1a) consisting of full-resolution elemental intensity rasters for the elements of interest (Ca, Na, K,
218 Mg, Fe and Ti). These rasters contain the X-ray counts of elemental intensity at each pixel and have a mean size
219 of over 20 megapixels over the 14 study thin sections. We selected these elements because they are present in
220 varying abundance in the mineral phases within the Rio Blanco tonalite, and hence are useful for distinguishing
221 among the mineral phases in these samples. For example, K, Mg, Fe, and Ti are present at high abundance in
222 biotite (Dong et al., 1999) but are present at low abundance in other major mineral phases in this lithology (e.g.,
223 plagioclase feldspar, quartz). Our initial attempts at classification showed that the inclusion of rasters of Si and Al
224 had no effect on classification accuracy, so we did not include them here.

225



226 This method requires a list of mineral phases present in the samples for both training of and prediction by the RF
227 models (Steps 4 and 5 in Section 2). Such a list can be obtained in a variety of ways, including prior studies of
228 qualitative mineralogy of the host lithology or mineral identification from optical microscopy on the sample thin
229 sections. For the 14 samples analyzed here, we generated a list of mineral phases by inspecting the EDS-
230 generated X-ray spectral data within Oxford AZtec, a proprietary software package integrated with the SEM that
231 we used to measure EDS scans of our samples. From these spectra we identified plagioclase feldspar, quartz,
232 hornblende, biotite, potassium feldspar, Fe-Ti oxides (predominantly magnetite-titanomagnetite), and apatite as
233 mineral phase classes for the RF models (Section 3.3). For those without offline access to a full EDS
234 environment, some systems such as Oxford AZtec allow for the full export of data into text or binary formats,
235 which can be accessed with free and open-source tools (e.g., HDFView or NIST DTSA-II). Due to trace
236 abundance (Murphy et al., 1998), other minerals present in the samples like epidote and titanite lacked an
237 adequate number of trainable examples, so were neglected or combined with an associated phase, Fe-Ti,
238 respectively. For reference, the mean abundance of apatite, the lowest abundance mineral phase we trained, was
239 ~0.1%. We recommend that phases present at abundances lower than this be omitted or combined.

240

241 **3.3 Smoothing and virtualization of the elemental intensity rasters**

242 We smoothed each elemental intensity raster with a 7-pixel radius circular mean filter using SAGA's Simple
243 Filter tool to eliminate noise in the EDS data. We chose this filter size because it optimized the accuracy
244 calculated during the training and validation of the RF model. We test the sensitivity of this choice in Section 4.3.
245 We then used the GDAL `gdalbuildvrt` command within QGIS to group the smoothed elemental intensity rasters
246 into a virtual raster dataset, in which each elemental raster is represented as a separate band. A virtual raster is a
247 container for multiple rasters that encodes metadata such as file locations and other attributes in extended markup
248 language (XML) (McInerney and Kempeneers, 2014). Opening and processing virtual raster datasets requires
249 less computer resources as the underlying rasters are only accessed when required.

250

251 **3.4 Training random forest models for mineral classification**

252 Before a RF model can be tasked with assigning a mineral phase to every pixel in an entire thin section, it must
253 first be trained upon the mineral phases in the thin section. On each of the virtual rasters for the 14 thin sections,
254 we selected an area encompassing less than ~15% of the total thin-section sample area within which we trained
255 the model. We selected training areas that represented all mineral phases as well as possible, so that each phase
256 would receive an adequate amount of training data for each phase. Selecting a small training area in the thin



257 section is useful because it enables users to test the accuracy of the trained model on other areas of the thin
258 section, if desired. This is not a necessary step in the method, but in Section 4 we show how such accuracy tests
259 can be done on other portions of the thin sections.

260

261 For each mineral phase within the training area, we manually generated hundreds of circular polygons upon the
262 virtual raster using the knowledge gained previously from examining the EDS spectra (Fig. 1). A single training
263 polygon within the training area collects all pixel values contained within it from each elemental intensity raster
264 composing the virtual raster. This polygon is then labelled as a single mineral phase, effectively labelling every
265 pixel value contained within it to that mineral phase. For a few thin sections, multiple subareas composed the
266 training area to incorporate enough data on less abundant minerals like apatite. Because each training polygon
267 encompassed pixel-level data for all bands from the virtual raster, the training datasets were large ($>10^5$ pixel-
268 level samples for each thin section). Training samples per mineral phase were highly unbalanced (i.e., some
269 mineral phases covered many more pixels than others) due to the high abundances of quartz and plagioclase
270 relative to those of minor mineral phases like apatite. Orfeo Toolbox handles this potential problem automatically
271 by randomly selecting samples at a rate relative to the size of the smallest class, ensuring that the minority classes
272 like apatite have an equal probability of being drawn into a sample subset used to construct an individual decision
273 tree.

274

275 Using the training data obtained from the virtual raster for each thin section, we trained RF image classification
276 models using the TrainImagesClassifier function in Orfeo Toolbox. In this function, users must select
277 hyperparameter values for the RF model. In machine learning, hyperparameters define the general behaviour of a
278 model, and are distinct from model parameters, which are learned through training. For more details about RF
279 machine learning models hyperparameters, see the review in Probst et al. (2019). We used the default
280 hyperparameter values (Table 1) for the models employed for our final predicted mineral maps.

281

282 A measure of model accuracy is automatically calculated by the TrainImagesClassifier function at this step using
283 unseen training data, which can be useful to examine before proceeding as to ensure that the RF model is
284 operating correctly. The accuracy metric we focus on in this study is the F1 score (Equation 3), which is the
285 harmonic mean of the precision metric (Equation 1) and the recall metric (Equation 2). This is a useful measure
286 of the accuracy of RF-predicted mineralogy because it penalizes false positives and false negatives while



287 rewarding true positives and neglecting true negatives (Chinchor and Sundheim, 1993), which can be very
288 plentiful for low abundance phases.

289

$$Precision = \frac{True\ positives}{True\ positives + False\ positives} \quad (1)$$

290

$$Recall = \frac{True\ positives}{True\ positives + False\ negatives} \quad (2)$$

291

$$F1\ score = \frac{2(Precision)(Recall)}{Precision + Recall} \quad (3)$$

292

293 In the application of Equations 1-3 to mineral maps, a true positive is defined as pixel-level agreement on the
294 presence of a given mineral phase between the model prediction and unused training data, which the algorithm
295 holds out from training for the purpose of calculating metrics such as the F1 score. Similarly, a true negative is
296 agreement on the absence of a given mineral phase. False positives and false negatives are disagreements on the
297 presence and absence of a given mineral phase, respectively. Application of the default hyperparameters to our
298 samples yielded very high F1 scores (~0.99). This gave us confidence that the predicted mineral maps generated
299 using the default hyperparameters were near optimal for comparison with manually delineated test maps
300 (described in Section 4.1).

301

302

Table 1. Default hyperparameter values for Orfeo Toolbox RF machine learning model.

Parameter name	Value
Maximum number of trees in the forest	100
Maximum depth of tree	5
Size of the randomly selected subset of features at each tree node	(number of features) ^{1/2}
Minimum number of samples at each node	10

303

304



305 We applied each trained model to its corresponding virtual raster to predict a single mineral phase at each pixel,
306 except in the case of ensemble voting ties, in which case no phase was assigned to that pixel. This resulted in
307 mineral maps at the same resolution as the virtual rasters ($\sim 4 \mu\text{m}$).

308

309 **3.5 Using the random forest models to generate mineral maps**

310 In our application of the trained RF models to our thin sections, the models calculated the entire thin-section scale
311 mineral maps in a under a minute using a desktop computer (4 GHz processor; 64 GB memory). Figure 1 shows
312 an example of one of these mineral maps.

313

314 After a thin section's mineral map has been generated, it is trivial to calculate the abundance of each mineral
315 phase by counting pixels. Figure 2 shows the abundance of each mineral phase across all 14 samples with the
316 error given by the mean F1 scores of the minerals. It also reveals relatively little variation in each mineral phase's
317 abundance among the 14 samples, which is consistent with previous observations of the Rio Blanco tonalite. The
318 RF-predicted mineral abundances compare well with those measured from modal analysis via point counting on
319 BSE imagery (Buss et al., 2008) and via quantitative XRD (Ferrier et al., 2010). Buss et al. (2008) measured
320 average areal abundances of 19.9% and 49.3% for quartz and plagioclase, respectively, comparable to the RF-
321 predicted average abundances of $22.8 \pm 1.0\%$ and $55.8 \pm 2.3\%$ (\pm error from mean F1 scores) on our 14 thin
322 sections. The combined abundance of hornblende and biotite ('Fe-silicates') measured by Buss et al. (2008) was
323 24%, which is close to the maximum RF-predicted abundance of 'Fe-silicates' among our 14 samples ($25.0 \pm$
324 1.5%). Using common values for molar masses (M mol^{-1}) and densities (M L^{-3}), the XRD-based abundances
325 (converted to areal abundance) from Ferrier et al. (2010) for quartz, plagioclase, and hornblende were 24%, 62%,
326 and 14%, respectively, while the RF-predicted mineral maps yielded $22.8 \pm 1.0\%$, $55.8 \pm 2.3\%$, and $10.4 \pm 0.7\%$,
327 respectively. When quartz, plagioclase, and alkali feldspar abundances are normalized for usage with a Quartz-
328 Alkali Feldspar-Plagioclase-Feldspathoid diagram (Le Maitre, 2002), the RF-predicted abundances for each
329 mineral phase demonstrated that all samples can be classified as tonalite, matching the name of the lithology.

330

331

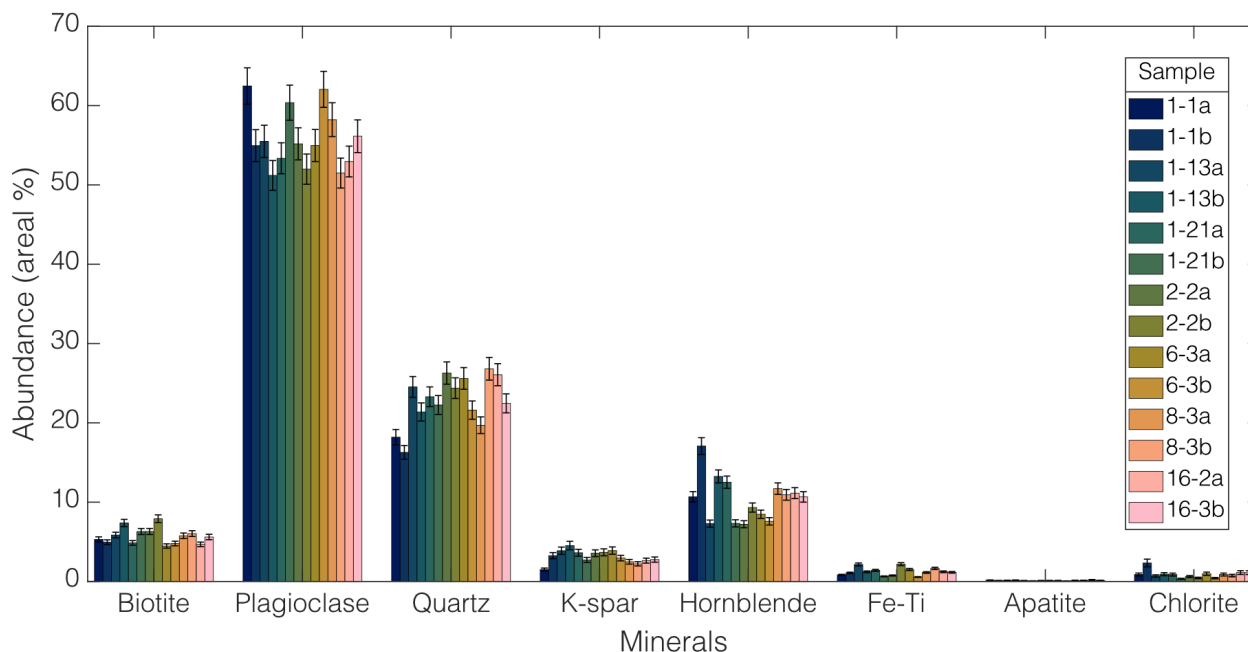


Figure 2. Areal abundance for all 14 samples of the Rio Blanco tonalite. Error bars stem from mean F1 scores for each individual mineral phase from test map comparisons (see Section 4.1).

332

333 4. Accuracy of random forest-predicted mineral maps and sensitivity analyses

334

335 4.1 Accuracy of random forest-predicted mineral maps

336 Before applying the trained RF models to the full thin sections, we manually mapped the mineralogy of a small
337 section for three samples (6-3a, 16-2a, and 1-13a) to assess the accuracy of the model-generated mineral maps.

338 We refer to these manually delineated mineral maps as “test maps”. These test maps were manually delineated as
339 vector polygons for all mineral phases using the elemental intensity rasters for guidance. For example, when
340 mapping a grain of potassium feldspar, we determined the boundaries of the grain with filtered and unfiltered
341 rasters of K as well as combined intensity rasters of multiple elements. We consider these maps to be ‘ground
342 truth’ data, which are never perfect representations of reality (Foody, 2024), but, nonetheless, may serve to
343 compare the performance of this method to the extremely slow process of manually mapping grain boundaries.
344 We then rasterized the manually-delineated vector maps, which resulted in the classification of every pixel within
345 the test maps as one of the eight mineral phases. The test maps averaged over 1 million pixels in size.

346



347 We compared the same section of the predicted mineral maps to the test maps using a frequency-weighted F1
348 score (Equation 4) to gauge the average accuracy for all mineral phases. To calculate a frequency-weighted F1
349 score, the F1 score for the i^{th} class (F1 score $_i$) is weighted by the class frequency (w_i), which is the proportion of
350 pixels of class i to the total number of pixels in the test map. Here, N is the number of mineral phases.

351

$$\text{Frequency-weighted F1 score} = \sum_{i=1}^N w_i \text{F1 score}_i \quad (4)$$

352

353 We clipped the portion of the predicted mineral map overlapping the test map from the full map for each of the
354 three thin sections with a test map. From these two rasters, we calculated the frequency-weighted F1 score.

355

356 How accurate were the RF-generated mineral maps in Section 3? For the three thin sections that were mapped
357 both manually and by the RF-based method in Section 2, the mean frequency-weighted F1 score among the three
358 thin sections was 0.948 ± 0.002 , meaning that nearly 95% of the pixels in the RF-predicted maps agreed with
359 those in the manually delineated maps (Table 2). The accuracy varied among mineral phases. The four most
360 abundant mineral phases (plagioclase, quartz, hornblende, and biotite) all have mean F1 scores of 0.94 to 0.96,
361 while apatite, the least abundant mineral phase, had the lowest mean F1 score of 0.72. A closer look at the
362 precision and recall metrics for apatite show that mean recall scores (0.62) were lower than mean precision
363 (0.91). This indicates that the models correctly predicted apatite when attempted but the models often neglected
364 to predict apatite. Abundance and the mean F1 score of a phase were not always linked; for example, Fe-Ti
365 oxides were low in abundance (~1%) but registered a mean F1 score of 0.91.

366

367 Figure 3 shows an example of an RF-predicted mineral map with misclassified pixels shown in red. This
368 illustrates a key point: the accuracy of the RF-predicted mineral maps is not spatially uniform. Most pixels that
369 diverge from manual classification occur at grain boundaries where elemental compositions shift abruptly in
370 space. By contrast, in mineral grain interiors, divergent pixels are far less common. This indicates that the
371 accuracy of RF-predicted mineralogy in grain interiors is higher than the F1 scores in Table 2.

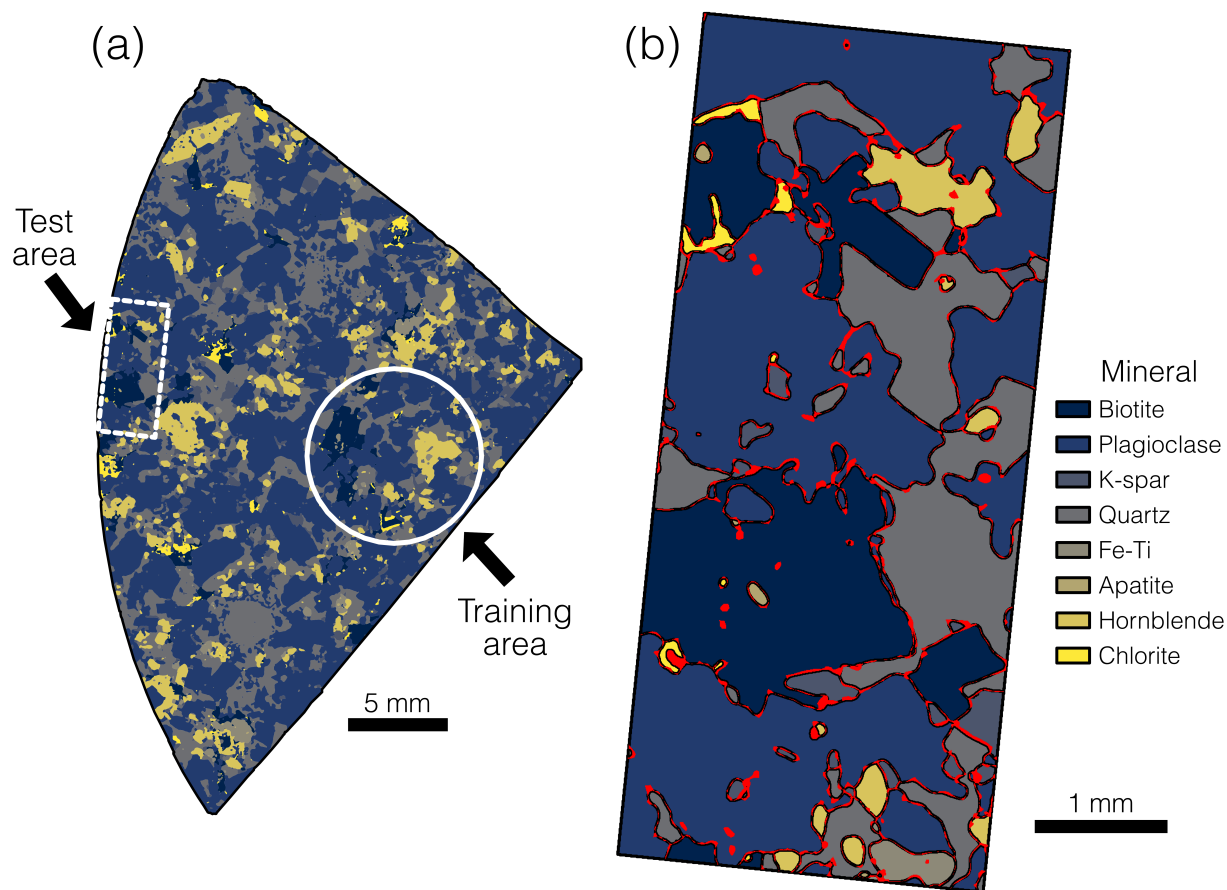


Figure 3. (a) Predicted mineral map for sample 6-3a, showing the location of the manually delineated test map, which we used to check accuracy. (b) Predicted mineral map for the test area. Red color signifies where pixels in the predicted map diverge from the manually delineated test map. This shows that most divergent pixels are at mineral grain boundaries.

372

373 A combined confusion matrix for pixel-level comparisons from every test and predicted map showed the most
374 common divergent classification was chlorite for biotite. This is likely because biotite and chlorite have similar
375 elemental compositions and because they often share a grain boundary (chlorite is a product of hydrothermal
376 alteration of biotite), which means they are more prone to disagreement along grain boundaries. Among the major
377 minerals, our models divergently classified potassium feldspar as plagioclase feldspar most often, likely because
378 many potassium feldspar grains in the Rio Blanco tonalite contain small amounts of Na, like plagioclase.

379



380 Figure 4 shows close agreement between the RF-predicted abundance and the manually mapped abundance in the
 381 test areas, with a mean difference for a given phase of $0.45 \pm 0.02\%$ across the three test maps. So, although some
 382 predicted pixels were misaligned spatially, the RF-predicted mineral abundances agree well with manual
 383 estimates derived from the test maps.

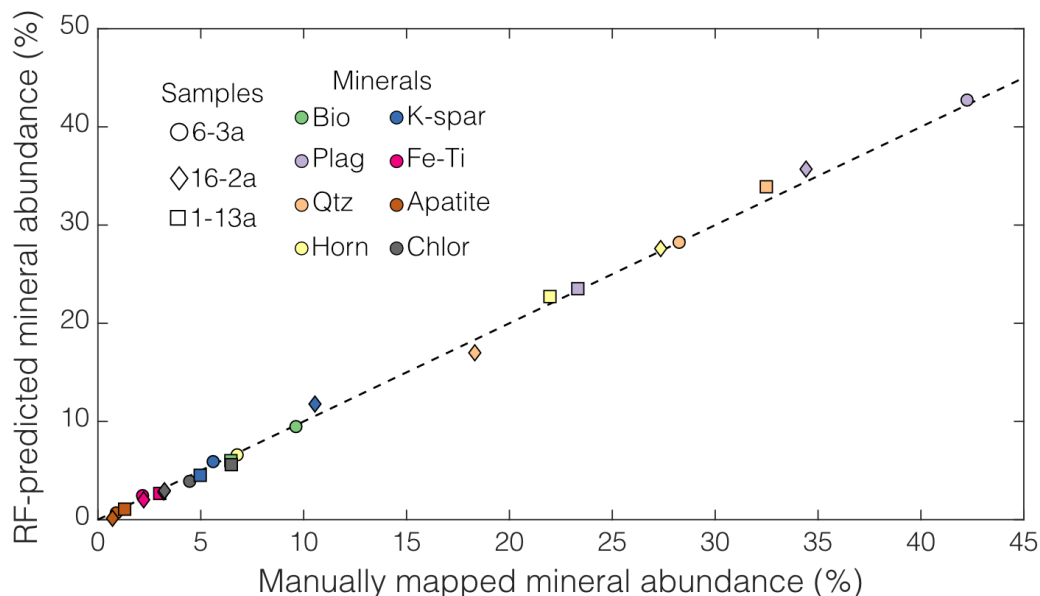


Figure 4. RF model-predicted mineral abundance vs. manually mapped mineral abundance in the test areas of the three samples with test maps. The dashed line is a 1:1 line. Although there was some spatial mismatch around the edge of mineral grains (e.g., Fig. 3), the RF-predicted modal abundances agree well with abundances inferred from manual mapping in the test areas.

384

385

Table 2. Mean F1 scores (accuracy metric) for mineral phases among the three test maps (Fig. 4), based on comparison of automated mineralogy maps to manually delineated mineralogy maps.

Mineral	Mean F1 score
All phases (frequency-weighted)	0.95
Plagioclase feldspar	0.96
Quartz	0.94
Hornblende	0.94



Biotite	0.94
Potassium feldspar	0.88
Fe-Ti oxides	0.91
Chlorite	0.79
Apatite	0.72

386

387 **4.2 Sensitivity of mineral maps to random forest hyperparameters and input features**

388 In our application of the method in Section 2 to the 14 samples in Section 3, we used a set of default values for
389 three RF hyperparameters: maximum tree depth, number of trees, and minimum sample size per node. Reviews
390 of hyperparameter tuning on RF models have shown that the number of trees and the minimum number of classes
391 per node can have a large effect on classification accuracy (Probst et al., 2019). How sensitive are the output
392 mineral maps to the user's choice of these hyperparameter values?

393

394 Orfeo Toolbox does not contain a facility for hyperparameter tuning in QGIS, so we developed a workflow to
395 undertake our own hyperparameter optimization outside of QGIS in Python. This is not a necessary step in the
396 method, but we have included this code in the Supplement for users who wish to conduct their own
397 hyperparameter optimization. We began by converting the smoothed elemental intensity image data in the three
398 training areas within the manually delineated test maps into NumPy arrays (Harris et al., 2020) using a
399 combination of three Python libraries: rasterio (Gillies et al., 2019), geopandas (Jordahl et al., 2020), and shapely
400 (Gillies et al., 2022). We then used the implementation of the RF classifier from the machine-learning package
401 scikit-learn (Pedregosa et al., 2011) for both hyperparameter optimization using a randomized five-fold cross
402 validation (Breiman and Spector, 1992) and derivation of feature importance using permutation testing (Breiman,
403 2001). Through these operations we seek to find optimal hyperparameters and test the importance of input
404 features (here, elements), respectively.

405

406 We used the scikit-learn RandomizedGridCV function to systematically test the sensitivity of the output mineral
407 maps to the RF hyperparameter values. To do this, we trained 100 unique RF models across a range of maximum
408 tree depth (1-100), number of trees (10-2000), and minimum sample size per node (5-25). These hyperparameters
409 are common between the Orfeo Toolbox and scikit-learn implementations of the RF classifier. We used five-fold
410 cross-validation, in which each randomly selected set of hyperparameters is used to train the same model five



411 times while sampling different portions of the training data (Breiman and Spector, 1992). We report the best fit
412 parameters and resultant accuracy in terms of the frequency-weighted F1 score upon comparison to the test maps
413 using these optimized parameters.

414

415 Orfeo Toolbox has not yet incorporated a capacity to derive feature importance scores. Feature importance in RF
416 classification is calculated by permutation testing, which is the extent to which an accuracy metric declines if a
417 single input feature's unused training data is randomly altered during the training process and validation process
418 (Breiman, 2001; Guo et al., 2011). We used the sci-kit learn function `permutation_importance` to assess
419 importance using the frequency-weighted F1 score. We report the feature importance for the three samples with
420 manually delineated test maps and discuss their implications.

421

422 Tuning the hyperparameters in scikit-learn showed that both a higher maximum tree depth and number of trees
423 may be optimal for our RF models, while the minimum sample for splitting was more variable (Table 3). Using
424 these optimized RF hyperparameters within Orfeo Toolbox yielded a mean frequency-weighted F1 score of 0.95
425 when comparing the three samples with manually delineated test maps, which is the same F1 score realized by
426 using the default hyperparameters. As the two implementations of the RF classifier are somewhat different in
427 terms of available hyperparameters, the comparison is imperfect, but does provide a check to see if the default
428 hyperparameters could be improved upon. That an optimized set of hyperparameters delivered very little to no
429 increase in accuracy is unsurprising as RF models are known to perform well with little to no tuning if reasonable
430 hyperparameter values are initially used (Maxwell et al., 2018). Unless low F1 scores are realized during Step 4,
431 it is our recommendation that the default RF hyperparameters in Orfeo Toolbox be used.

432

433

Table 3. Optimal RF hyperparameters from five-fold cross validation performed using sci-kit learn.

Sampl e	Maximum tree depth	Number of trees	Minimum sample for split
1-13a	73	1685	25
6-3a	94	1371	5
16-2a	73	1581	5

434



435

436 Feature importance, as determined through permutation testing, showed that both K and Mg were the most
437 important features for our scikit-learn trained models with mean decreases in accuracy based on frequency-
438 weighted F1 scores derived from the training and validation process on unused data of 0.29 for both elements
439 (Fig. 5). Ti was relatively unimportant with a very small, slightly positive value, implying it could be omitted.
440 Although Ti is present within biotite and Fe-Ti oxides in our samples, Ti showed little to no decrease in mean
441 accuracy as both biotite and Fe-Ti oxides can be classified using other elements. We tested whether our feature
442 importance scores were pertinent to models in Orfeo Toolbox by leaving out, in turn, K, Mg, and Ti during
443 training and validation process. Excluding K decreased mean F1 scores due to the degradation of potassium
444 feldspar, biotite, and chlorite accuracy. In contrast, omitting Mg did not decrease F1 scores, showing that a
445 feature importance score does not directly translate to decreased model accuracy upon omission (Cutler et al.,
446 2011). Leaving out Ti had little effect on F1 scores. If a user of our method is unsure whether an element could
447 be a truly important feature, omitting an important element from the training process by creating virtual rasters
448 without that element should yield a notable degradation in training F1 scores.

449

450

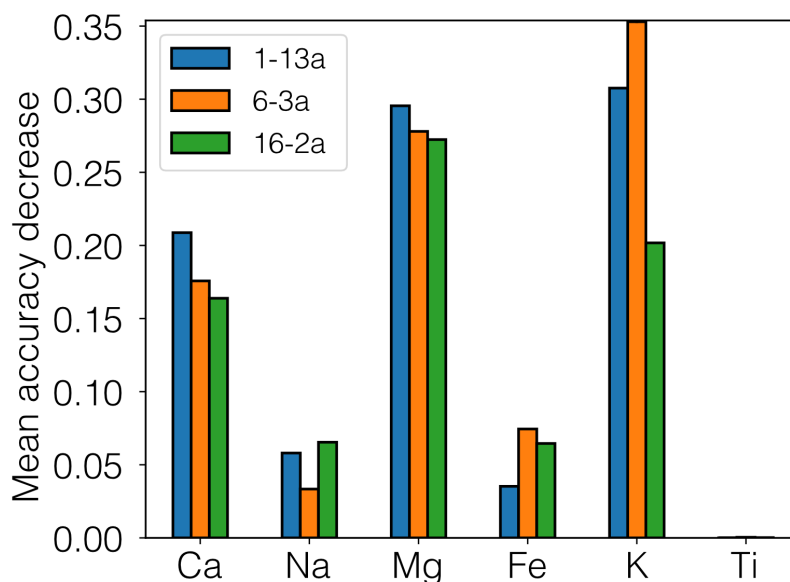


Figure 5. Feature importance from scikit-learn using permutation testing for all six input elements for the three samples with test maps. Mean accuracy decrease is the change in the F1 score due to



randomly changing feature data in the unused portion of the training data during the validation process. In Orfeo Toolbox, training models that omitted K degraded F1 scores while those that omitted Mg yielded little change, indicating that feature importance score does not always directly map onto model accuracy and that some experimentation with input features (elements) during the training phase is warranted.

451

452 **4.3 Sensitivity of mineral maps to filter sizes**

453 In our application of this method to our samples, we applied a circular, 7-pixel radius mean filter to the EDS-
454 generated elemental intensity rasters (Step 2 in Section 2), and we applied a circular, 10-pixel radius majority
455 filter to the output mineral maps (Step 6). To quantify the sensitivity of the output mineral maps to these
456 “hidden” parameters, we generated a series of RF models across a range of mean filter radii for the elemental
457 intensity rasters (no filter, 2, 5, 7, 10, and 20 pixels) and a range of majority filter radii (no filter, 2, 5, 7, 10, and
458 20 pixels). For the three thin sections with manually delineated mineral maps, we calculated the frequency-
459 weighted F1 score of the entire thin section by comparing each of the RF-predicted mineral maps to the manually
460 delineated test maps.

461

462 Figure 6 reveals that both the mean filter and the majority filter affect the accuracy of the predicted mineral maps.
463 The largest impact on the accuracy, as measured by F1 score, was in the application of any mean filter at all to
464 the input elemental intensity rasters. The left panel in Fig. 6 shows that applying no mean filter to the elemental
465 intensity rasters produced low F1 scores (0.52-0.69) for all models and all samples, regardless of the size of the
466 majority filter. Accuracy increased with mean filter radius up to 5 and 7 pixels, which yielded high F1 scores at
467 all majority filter sizes (0.91-0.96) due to the elimination of spurious inclusions within larger mineral grains
468 (middle panels in Fig. 6). Beyond that size, accuracy decreased slightly with higher mean filter radius, with lower
469 F1 scores at radii of 10 pixels (F1 scores of 0.90-0.95) and 20 pixels (0.87-0.89). This implies an intermediate
470 optimal mean filter radius of 5-7 pixels for these samples.

471

472 Accuracy was sensitive to the size of the majority filter, particularly for models that applied no mean filter or a
473 small (2-pixel radius) mean filter to the input elemental intensity rasters (Fig. 6). For the models that applied a
474 mean filter of any size, accuracy was lower at small majority filter radii (0 or 2 pixels) and large radii (20 pixels)
475 than at intermediate majority filter radii (5-10 pixels). At the largest radii, the RF-predicted mineral grains begin
476 to lose shape, becoming more circular. Thus, accuracy was maximized at intermediate majority filter radii of 5-7



477 pixels, just as it was at intermediate mean filter radii. Excluding plagioclase and quartz (which generally do not
 478 occur as isolated grains), the three samples with test maps (6-3a, 1-13a, and 16-2a) have a median grain area of
 479 $\sim 0.005 \text{ mm}^2$ ($n = 5188$ mineral grains across all three samples) while the 5-7-pixel radii filters have areas of
 480 $\sim 0.001 \text{ mm}^2$ and $\sim 0.002 \text{ mm}^2$, respectively. These optimal sizes most likely result from a mix of the initial EDS
 481 pixel resolution and data quality and the types and sizes of minerals in the thin section (Lanari et al., 2014;
 482 Ortolano et al., 2018), so we recommend that users experiment to find the optimum filter sizes for their samples.
 483
 484

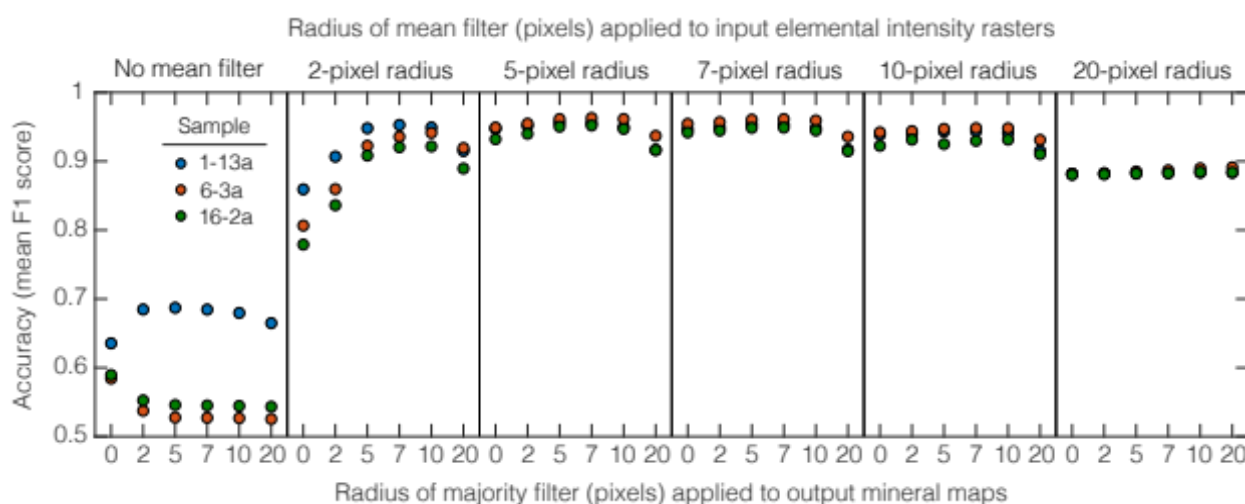


Figure 6. Accuracy of the output mineral maps (as quantified by frequency-weighted mean F1 scores) for combinations of mean filter and majority filter sizes for the three samples with test maps. Each section is a single mean filter size. The most accurate mineral maps (i.e., those with the highest F1 scores) were generated using a 5- or 7-pixel radius mean filter combined with a 5- or 7-pixel radius majority filter.

485

486

487 5 Discussion

488

489 5.1 Advantages of this open-source automated mineralogy method

490 Situating our workflow in a free and open-source GIS environment confers several practical benefits. Both Orfeo

491 Toolbox and QGIS are frequently updated with source code that can be examined and modified, unlike many



492 proprietary hardware/software systems (Keulen et al., 2020). Orfeo Toolbox and QGIS each have extensive
493 documentation and user forums monitored by the developers, which can aid in addressing user issues (Raza and
494 Capretz, 2015). Incorporating open-source software into scientific methods fosters transparency and
495 reproducibility as the software is widely accessible and more easily scrutinized (Ramachandran et al., 2021). As
496 both Orfeo Toolbox and QGIS are ongoing efforts with active contributing communities, our no-code workflow
497 is tied to software that is not likely to fall into disrepair or unavailability, unlike much open-source scientific
498 software (Coelho et al., 2020). Furthermore, both Orfeo Toolbox and QGIS are available for all major operating
499 systems, Windows, macOS (Intel), and Linux, so this factor does not limit accessibility. Orfeo Toolbox will
500 likely continue to incorporate new state-of-the-art, machine-learning algorithms. For example, Orfeo Toolbox has
501 recently been unofficially extended to utilize the Google TensorFlow library (Abadi et al., 2016) to perform deep-
502 learning tasks on remote sensing imagery (Cresson, 2018, 2022). There are also efforts to develop open-source
503 scanning electron microscope systems and attendant software such as the NanoMi project (Malac et al., 2022).
504 All of this means that automated mineralogy methods are likely to become more popular and accessible.

505

506 We expect that a broad range of geoscientists will be capable of using this GIS-based method, since many
507 geoscience undergraduate programs incorporate GIS into courses (Marra et al., 2017). It requires no
508 programming skill to obtain mineral maps, thereby eliminating a potential barrier for use (Bowlick et al., 2016).
509 Since the workflow takes place within a GIS environment, the input elemental intensity rasters could easily be
510 processed in other ways besides the mean smoothing filter that we applied here, such as edge-detection filtering
511 or elemental intensity ratioing. Creation of optimal input features, so-called feature engineering, is fostered by the
512 many QGIS frontends that interface with SAGA GIS and GDAL raster manipulation programs. Our method does
513 not require a corresponding plugin for Orfeo Toolbox/QGIS, but much of it could be automated from the Orfeo
514 Toolbox/QGIS Python API or as QGIS console commands, if desired. Input parameters for image filters and
515 hyperparameters for the RF models can be saved as JavaScript Object Notation (JSON) files, which can be
516 loaded in later, overcoming some of the reproducibility issues inherent in workflows using graphical user
517 interfaces (Brundson, 2016).

518

519 **5.2 Illustration of the utility of random forest-generated mineral maps**

520 There are many potential uses for thin section-scale mineral maps once they have been generated. Converting the
521 mineral maps into vector form allows for the calculation of derived parameters such as median grain area for
522 minerals that occur as single grains (e.g., biotite), distance between grains of a mineral, and the types of minerals



523 surrounding a grain or grains in the case of abundant, connected minerals like plagioclase and quartz. This type of
524 data is normally generated by proprietary automated mineralogy systems but could aid in geoscience disciplines
525 beyond ore geology or petroleum geology (Han et al., 2022). An illustrative example is in the analysis of grain-
526 scale properties of biotite. This is of wide interest because oxidation of ferrous Fe in biotite drives expansion of
527 biotite grains, which generates stresses in the surrounding rock that may be large enough to fracture the rock
528 (Fletcher et al., 2006; Goodfellow et al., 2016; Goodfellow and Hilley, 2022). To the extent that biotite expansion
529 promotes generation of regolith from bedrock, it may even influence the km-scale evolution of mountainous
530 topography (Wahrhaftig, 1965; Xu et al., 2022). In granitic rocks, numerical modelling has shown that biotite
531 abundance influences the accrual of microscale damage (Shen et al., 2019) and weathering profile development is
532 partially guided by biotite crystal size (Goodfellow and Hilley, 2022). These are two properties that can be
533 directly measured in our thin section-scale mineral maps.

534

535 To obtain such mineral maps in some previous studies, researchers have often engaged in manual or semi-
536 automated characterizations of sample mineral properties (Buss et al., 2008; Ündül, 2016). These workflows are
537 often tailored for a single study (e.g., Goodfellow et al., 2016). Methods that are based on generalizable
538 workflows involving automated mineralogy methods such as the one presented in this study could enhance
539 comparability between studies. Since we converted the predicted mineral maps into a vector (polygon) form
540 within QGIS, we could use built-in functions to gather large amounts of data on grain neighbours or perform
541 grain size measurements. For example, the 20 largest biotite grains in samples 1-1a and 6-3b comprise 80% and
542 94% of the total biotite area, respectively (Fig. 7a-b). The median grain area of these 20 biotite grains in sample
543 1-1a is 0.60 mm^2 , several times larger than that in sample 6-3b (0.19 mm^2 ; Fig. 7c).

544

545 We can also use raster morphology operations on the mineral maps to measure distances between mineral phases.
546 In analog and numerical experiments that impose stress on granitic rocks (Tapponier and Brace, 1976; Li et al.,
547 2003; Mahboudi et al., 2012), biotite grains can act as preferential origination points for microfractures, but
548 biotite can also arrest propagation of microfractures arising from neighboring grains. Thus, the distance between
549 biotite grains may be an important, yet rarely measured property. In the example of the two samples in Fig. 7,
550 biotite grains have similar median distances from one another but different probability distributions of distances
551 between biotite grains, particularly in the long tail of the distributions at larger distances (Fig. 7e). We can also
552 extract the composition of neighbouring grains surrounding biotite (Fig. 7f), which reveal that chlorite is much
553 more abundant near biotite relative to the rest of the thin section. Data like these can be useful for those studying



554 the impacts of different grain-grain contacts on stress response during rock mechanics experiments (e.g., Aligholi
 555 et al., 2019), which has shown that some mineral interactions can have an outsized influence on the development
 556 of fractures and failure. In sum, the data in Fig. 7 illustrate the potential power of RF-generated mineral maps to
 557 improve quantitative in-situ investigations of biotite weathering (Behrens et al., 2021) and form the basis for
 558 more realistic models of biotite-driven rock damage (Shen et al., 2019).
 559

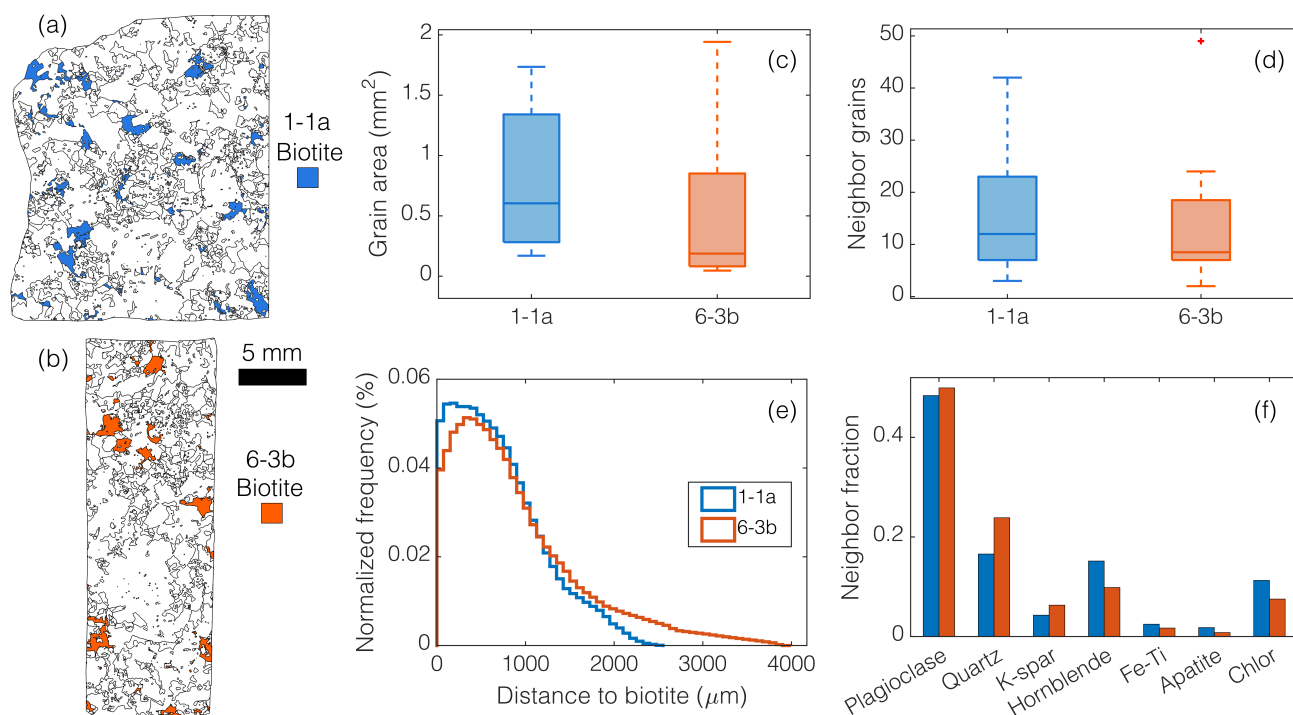


Figure 7. Example of quantities that can be obtained from mineral maps generated by the automated method in this study. (a-b). Colours highlight biotite grains identified in the RF-generated mineral maps in thin sections 1-1a (blue) and 6-3b (orange). (c-f). Biotite properties extracted from predicted maps for the 20 largest biotite grains in each sample. These data could help inform numerical models of microcrack generation and allow for quantitative comparisons between different samples or lithologies (e.g., Shen et al., 2019). (c) Boxplot of biotite grain area (mm^2) for the 20 largest biotite grains for both samples. (d) Boxplot of number of grains surrounding the largest 20 biotite grains. (e) Normalized frequency distribution of distances between biotite pixels (not including those inside a biotite grain). (f) Composition of neighbours as a fraction of perimeter.

560

561



562 **5.3 Limitations**

563 Our method's greatest asset is that it can generate thin section-scale mineral maps without requiring the use of
564 propriety software or a background in programming. Its most important limitation is that it is most accurate if the
565 user trains a RF model for every thin section sample. Using a RF model that was trained on one sample to predict
566 mineral maps for another sample can yield mineral maps that accurately map mineral phases in some areas but
567 inaccurately in others. For example, when we applied a RF model that was trained on sample 16-2a to sample 6-
568 3a, apatite abundance was overpredicted by a factor of 5 possibly due to 6-3a having some highly calcic zones
569 within plagioclase grains. So, for the most accurate results, we recommend training each thin section separately.
570

571 A second limitation is that this method tends to be less accurate at identifying low abundance phases. Unlike
572 some proprietary automated mineralogy software systems, our method does not use predefined EDS spectra to
573 identify mineral phases. Instead, our method trains RF models on the samples themselves, which means that each
574 mineral phase of interest must be abundant enough to properly train the RF model. The relatively low F1 scores
575 of the lower abundance phases in our samples (Table 2) suggest that the minimum abundance required to train a
576 RF model is larger for minerals with small grain size (e.g., in the case of apatite) and a lack of compositional
577 distinction (e.g., in the case of chlorite). Mineral phases must be resolvable by the EDS data, so collecting EDS
578 data with a field-emission-gun SEM at higher resolution ($\sim 0.1 \mu\text{m}$) could improve mineral classification in rocks
579 with finer grain size distributions (Han et al., 2022).

580
581 A final limitation is that mineral grains that border mineral grains of the same phase appear to the RF model as
582 regions of the same mineral, and hence can be classified as a single mineral grain, rather than two grains. This is
583 a common issue shared with other automated mineralogy methods (Lanari et al., 2014; Hrtska et al., 2019), and it
584 can affect inferred probability distributions of mineral grain size of those mineral phases if not properly
585 accounted for.

586

587 **6. Conclusions**

588 The main contribution of this study is a new automated method for obtaining mineral maps from EDS scans of
589 rock thin sections. This method is implemented within a free and open-source GIS application, uses free and
590 open-source plugins for RF image classification, and requires no programming. To demonstrate the utility of this
591 method, we trained RF models on EDS scans of 14 thin-section samples of a well-studied, plutonic igneous rock.
592 The resulting model-predicted mineral maps compare well with manually delineated mineralogy maps, with 95%



593 of pixels on the mineral maps predicted correctly. With regards to the most abundant minerals in the Rio Blanco
594 tonalite, plagioclase feldspar and quartz, the models attained 96% and 94% accuracy, respectively.

595

596 We utilized scikit-learn's implementation of the RF classifier to search for optimal RF hyperparameters and to
597 test input feature (element) importance. We saw no increase in accuracy using optimal hyperparameters found in
598 scikit-learn when used within Orfeo Toolbox, so we recommend using the default hyperparameters. We did see
599 that an important input feature, K, did lower accuracy when not included in Orfeo Toolbox-based models, so
600 some level of experimentation with input features during the training step is warranted. We also tested to see if
601 our pre- and post-processing steps had a large influence on accuracy by using different sizes of mean and
602 majority filters. An absence of filtering and excessively large filters led to lower accuracy while filters in the
603 range of 5-10 pixels for both mean and majority filters led to higher accuracy.

604

605 Situating the workflow within a free and open-source GIS environment confers distinct advantages. Open source
606 extends benefits such as source code availability, extensive documentation, and accessibility. Moreover, as the
607 workflow is within a GIS environment, the application is likely to be familiar to a range of geoscientists. Also, all
608 the available tools (e.g., different types of image filters) within the GIS allow for easy input feature
609 experimentation. The mineral maps from our method proved highly accurate when compared to manually-
610 delineated maps, and estimates of mineral abundance compared well to previous estimates from the literature for
611 our sample lithology. Many of the measured quantities produced by proprietary automated mineralogy systems
612 are obtainable once predicted mineral maps are converted to vector datasets. These measurements, such as
613 median grain size and amount of grain neighbours, can be useful to researchers studying microscale damage
614 processes that arise through rock weathering or rock mechanics experiments. We hope that this method will be
615 useful for researchers who wish to obtain rapid, automated mineralogy maps of thin sections.

616

617 **Code and Data availability**

618 The manuscript supplement containing the code for analysis and visualizations is available through a Zenodo
619 repository (<https://zenodo.org/doi/10.5281/zenodo.10912627>; Reed et al., 2024). The supplement also contains
620 data (smoothed elemental intensity rasters, training polygons, and test maps) for the three thin sections with
621 manually delineated test maps.

622

623 **Author contribution**



624 **Miles Reed**: conceptualization, formal analysis, methodology, software, visualization, and writing (original draft
625 and preparation); **Ken Ferrier**: funding acquisition, supervision, visualization, and writing (review and editing);
626 **William Nachlas**: resources and writing (review and editing); **Bil Schneider**: investigation and writing (review
627 and editing); **Chloe Arson**: funding acquisition and writing (review and editing); **Tingting Xu**: writing (review
628 and editing); **Xianda Shen**: writing (review and editing); **Nicole West**: funding acquisition and writing (review
629 and editing).

630

631 **Competing interests**

632 The authors declare no competing interests.

633

634 **Acknowledgements**

635 This work was supported by NSF award EAR-1934458 and NSF award EAR-1755321.

636

637 **References**

- 638 Abadi, M., Agarwal, A., Barham, P., Brevdo, E., Chen, Z., Citro, C., ... and Zheng, X: Tensorflow: Large-scale
639 machine learning on heterogeneous distributed systems. arXiv [preprint], [https://doi.org/10.48550/
640 arXiv.1603.04467](https://doi.org/10.48550/arXiv.1603.04467), 16 March 2016.
- 641 Aligholi, S., Lashkaripour, G. R., and Ghafoori, M: Estimating engineering properties of igneous rocks using
642 semi-automatic petrographic analysis. Bull. Eng. Geol. Environ., 78, 2299-2314. [https://doi.org/10.1007/s10064-
643 018-1305-7](https://doi.org/10.1007/s10064-018-1305-7), 2019.
- 644 Behrens, R., Wirth, R., and von Blanckenburg, F: Rate limitations of nano-scale weathering front advance in the
645 slow-eroding Sri Lankan Highlands, Geochim. Cosmochim. Acta, 311, 174-197, [https://doi.org/10.1016/
646 j.gca.2021.06.003](https://doi.org/10.1016/j.gca.2021.06.003), 2021.
- 647 Berrezueta, E., Domínguez-Cuesta, M. J., and Rodríguez-Rey, Á: Semi-automated procedure of digitalization and
648 study of rock thin section porosity applying optical image analysis tools, Comput. Geosci., 124, 14-26, [https://
649 doi.org/10.1016/j.cageo.2018.12.009](https://doi.org/10.1016/j.cageo.2018.12.009), 2019.
- 650 Bjørlykke, K: Relationships between depositional environments, burial history and rock properties. Some princi-
651 pal aspects of diagenetic process in sedimentary basins, Sediment. Geol., 301, 1-14, [https://doi.org/10.1016/j.sed-
652 geo.2013.12.002](https://doi.org/10.1016/j.sed-geo.2013.12.002), 2014.
- 653 Blannin, R., Frenzel, M., Tuşa, L., Birtel, S., Ivăşcanu, P., Baker, T., and Gutzmer, J: Uncertainties in quantitative
654 mineralogical studies using scanning electron microscope-based image analysis, Miner. Eng., 167, 106836,
655 <https://doi.org/10.1016/j.mineng.2021.106836>, 2021.
- 656 Breiman, L: Random forests, Mach. Learn., 45, 5-32, <https://doi.org/10.1023/A:1010933404324>, 2001.



- 657 Breiman, L., and Spector, P: Submodel selection and evaluation in regression: The X-random case, *Int. Stat.*
658 *Rev.*, 291-319, <https://doi.org/10.2307/1403680>, 1992.
- 659 Brocard, G., Willebring, J. K., and Scatena, F. N: Shaping of topography by topographically-controlled vegetation
660 in tropical montane rainforest, *PLoS One*, 18(3), e0281835, <https://doi.org/10.1371/journal.pone.0281835>, 2023.
- 661 Brunsdon, C: Quantitative methods I: Reproducible research and quantitative geography, *Prog. Hum. Geogr.*,
662 40(5), 687-696, <https://doi.org/10.1177/0309132515599625>, 2016.
- 663 Bürgmann, R., and Dresen, G: Rheology of the lower crust and upper mantle: Evidence from rock mechanics,
664 geodesy, and field observations, *Annu. Rev. Earth Planet. Sci.*, 36, 531-567, <https://doi.org/10.1146/annurev.earth.36.031207.124326>, 2008.
- 666 Buss, H. L., Sak, P. B., Webb, S. M., and Brantley, S. L.: Weathering of the Rio Blanco quartz diorite, Luquillo
667 Mountains, Puerto Rico: Coupling oxidation, dissolution, and fracturing, *Geochim. Cosmochim. Acta*, 72(18),
668 4488-4507, <https://doi.org/10.1016/j.gca.2008.06.020>, 2008.
- 669 Callahan, R. P., Riebe, C. S., Sklar, L. S., Pasquet, S., Ferrier, K. L., Hahm, W. J., ... and Holbrook, W. S.: Forest
670 vulnerability to drought controlled by bedrock composition, *Nat. Geosci.*, 15(9), 714-719, <https://doi.org/10.1038/s41561-022-01012-2>, 2022.
- 672 Callister, W. D., and Rethwisch, D. G.: *Callister's Materials Science and Engineering*, Global Edition, 10th Edi-
673 tion, John Wiley & Sons, ISBN 978-1-119-45520-2, 2019.
- 674 Chinchor, N., and Sundheim, B. M: MUC-5 evaluation metrics, in: *Proceedings of the Fifth Message Understand-*
675 *ing Conference (MUC-5)*, August 25-27, 1993, <https://doi.org/10.3115/1072017.1072026>, 1993.
- 676 Coelho, J., Valente, M. T., Milen, L., and Silva, L. L.: Is this GitHub project maintained? Measuring the level of
677 maintenance activity of open-source projects, *Inf. Software Technol.*, 122, 106274, <https://doi.org/10.1016/j.infsof.2020.106274>, 2020.
- 679 Comas, X., Wright, W., Hynek, S. A., Fletcher, R. C., and Brantley, S. L.: Understanding fracture distribution and
680 its relation to knickpoint evolution in the Rio Icacos watershed (Luquillo Critical Zone Observatory, Puerto Rico)
681 using landscape-scale hydrogeophysics, *Earth Surf. Processes Landforms*, 44(4), 877-885, <https://doi.org/10.1002/esp.4540>, 2019.
- 683 Conrad, O., Bechtel, B., Bock, M., Dietrich, H., Fischer, E., Gerlitz, L., ... and Böhner, J.: System for automated
684 geoscientific analyses (SAGA) v. 2.1. 4, *Geosci. Model Dev.*, 8(7), 1991-2007, <https://doi.org/10.5194/gmd-8-1991-2015>, 2015.
- 686 Cresson, R.: A framework for remote sensing images processing using deep learning techniques, *IEEE Geosci.*
687 *Remote Sens. Lett.*, 16(1), 25-29, <https://doi.org/10.1109/lgrs.2018.2867949>, 2018.
- 688 Cresson, R. (2022). SR4RS: A tool for super resolution of remote sensing images, *J. Open Res. Software*, 10(1),
689 <https://doi.org/10.5334/jors.369>, 2022.



- 690 Cutler, A., Cutler, D. R., and Stevens, J. R.: Random forests, in: Ensemble machine learning: Methods and appli-
691 cations, edited by: Zhang, C., and Ma, Y., Springer, 157-175, https://doi.org/10.1007/978-1-4419-9326-7_5,
692 2012.
- 693 Dong, H., Peacor, D. R., and Murphy, S. F.: TEM study of progressive alteration of igneous biotite to kaolinite
694 throughout a weathered soil profile, *Geochim. Cosmochim. Acta*, 62(11), 1881-1887, [https://doi.org/10.1016/
695 s0016-7037\(98\)00096-9](https://doi.org/10.1016/s0016-7037(98)00096-9), 1998.
- 696 Elghali, A., Benzaazoua, M., Bouzahzah, H., Bussière, B., and Villarraga-Gómez, H.: Determination of the avail-
697 able acid-generating potential of waste rock, part I: Mineralogical approach, *Appl. Geochem.*, 99, 31-41, [https://
698 doi.org/10.1016/j.apgeochem.2018.12.010](https://doi.org/10.1016/j.apgeochem.2018.12.010), 2018
- 699 Fandrich, R., Gu, Y., Burrows, D., and Moeller, K.: Modern SEM-based mineral liberation analysis, *Int. J. Miner.*
700 *Process.*, 84(1-4), 310-320, <https://doi.org/10.1016/j.minpro.2006.07.018>, 2007.
- 701 Ferrier, K. L., Kirchner, J. W., Riebe, C. S., and Finkel, R. C.: Mineral-specific chemical weathering rates over
702 millennial timescales: Measurements at Rio Icacos, Puerto Rico, *Chem. Geol.*, 277(1-2), 101-114, [https://
703 doi.org/10.1016/j.chemgeo.2010.07.013](https://doi.org/10.1016/j.chemgeo.2010.07.013), 2010.
- 704 Fletcher, R. C., Buss, H. L., and Brantley, S. L.: A spheroidal weathering model coupling porewater chemistry to
705 soil thicknesses during steady-state denudation, *Earth Planet. Sci. Lett.*, 244(1-2), 444-457, [https://doi.org/
706 10.1016/j.epsl.2006.01.055](https://doi.org/10.1016/j.epsl.2006.01.055), 2006.
- 707 GDAL/OGR contributors: GDAL/OGR Geospatial Data Abstraction Software Library. Zenodo [code], [https://
708 doi.org/10.5281/zenodo.5884351](https://doi.org/10.5281/zenodo.5884351), 2023.
- 709 Gillies, S., and others: Rasterio: geospatial raster I/O for Python programmers, GitHub [code], [https://
710 github.com/rasterio/rasterio](https://github.com/rasterio/rasterio), 2019.
- 711 Gillies, S., van der Wel, C., van den Bossche, J., Taves, M., Arnott, J., and Ward, B. C.: Shapely: Manipulation
712 and analysis of geometric objects in the Cartesian plane. Zenodo [code], <https://doi.org/10.5281/zenodo.5597138>,
713 2023.
- 714 Goldstein, J. I., Newbury, D. E., Michael, J. R., Ritchie, N. W., Scott, J. H. J., and Joy, D. C.: Scanning Electron
715 Microscopy and X-ray Microanalysis, 4th Edition, Springer, <https://doi.org/10.1007/978-1-4939-6676-9>, 2018.
- 716 Goodfellow, B. W., and Hilley, G. E.: Climatic and lithological controls on the structure and thickness of granitic
717 weathering zones, *Earth Planet. Sci. Lett.*, 600, 117890, <https://doi.org/10.1016/j.epsl.2022.117890>, 2022.
- 718 Goodfellow, B. W., Hilley, G. E., Webb, S. M., Sklar, L. S., Moon, S., and Olson, C. A.: The chemical, mechani-
719 cal, and hydrological evolution of weathering granitoid, *J. Geophys. Res.: Earth Surf.*, 121(8), 1410-1435,
720 <https://doi.org/10.1002/2016jf003822>, 2016.
- 721 Gottlieb, P., Wilkie, G., Sutherland, D., Ho-Tun, E., Suthers, S., Perera, K., Jenkins, B., Spencer, S., Butcher, A.,
722 and Rayner, J.: Using quantitative electron microscopy for process mineralogy applications, *JOM*, 52, 24-25,
723 <https://doi.org/10.1007/s11837-000-0126-9>, 2000.



- 724 Grizonnet, M., Michel, J., Poughon, V., Inglada, J., Savinaud, M., and Cresson, R. (2017). Orfeo ToolBox: Open
725 source processing of remote sensing images, *Open Geospatial Data, Software and Stand.*, 2(1), 1-8, [https://](https://doi.org/10.1186/s40965-017-0031-6)
726 doi.org/10.1186/s40965-017-0031-6, 2017.
- 727 Guo, L., Chehata, N., Mallet, C., and Boukir, S.: Relevance of airborne lidar and multispectral image data for ur-
728 ban scene classification using Random Forests, *ISPRS J. Photogramm. Remote Sens.*, 66(1), 56-66, [https://](https://doi.org/10.1016/j.isprsjprs.2010.08.007)
729 doi.org/10.1016/j.isprsjprs.2010.08.007, 2011.
- 730 Han, S., Löhr, S. C., Abbott, A. N., Baldermann, A., Farkaš, J., McMahon, W., Miliken, K., Rafiei, M., Wheeler,
731 C., and Owen, M.: Earth system science applications of next-generation SEM-EDS automated mineral mapping,
732 *Front. Earth Sci.*, 10, 956912, <https://doi.org/10.3389/feart.2022.956912>, 2022.
- 733 Harlov, D. E., Hansen, E. C., and Bigler, C.: Petrologic evidence for K-feldspar metasomatism in granulite facies
734 rocks, *Chem. Geol.*, 151(1-4), 373-386, [https://doi.org/10.1016/s0009-2541\(98\)00090-4](https://doi.org/10.1016/s0009-2541(98)00090-4), 1998.
- 735 Harris, C.R., Millman, K.J., van der Walt, S.J., Gommers, R., Virtanen, P., ... and Cournapeau, D.: Array pro-
736 gramming with NumPy, *Nature*, 585, 357–362. <https://doi.org/10.1038/s41586-020-2649-2>, 2020.
- 737 Hazen, R. M., Papineau, D., Bleeker, W., Downs, R. T., Ferry, J. M., McCoy, T. J., ... and Yang, H.: Mineral evo-
738 lution, *Am. Mineral.*, 93(11-12), 1693-1720, <https://doi.org/10.2138/am.2008.2955>, 2008.
- 739 Hilton, R. G., and West, A. J.: Mountains, erosion and the carbon cycle, *Nat. Rev. Earth Environ.*, 1(6), 284-299,
740 <https://doi.org/10.1038/s43017-020-0058-6>, 2020.
- 741 Hrstka, T., Gottlieb, P., Skala, R., Breiter, K., and Motl, D.: Automated mineralogy and petrology-applications of
742 TESCAN Integrated Mineral Analyzer (TIMA), *J. Geosci.*, 63(1), 47-63, <https://doi.org/10.3190/jgeosci.250>,
743 2018.
- 744 Hupp, B. N., and Donovan, J. J.: Quantitative mineralogy for facies definition in the Marcellus Shale (Ap-
745 palachian Basin, USA) using XRD-XRF integration, *Sediment. Geol.*, 371, 16-31, [https://doi.org/10.1016/j.sed-](https://doi.org/10.1016/j.sed-geo.2018.04.007)
746 [geo.2018.04.007](https://doi.org/10.1016/j.sed-geo.2018.04.007)
- 747 Jordahl, K., Van den Bossche, J., Wasserman, J., McBride, J., Gerard, J., Fleischmann, M., ... and Greenhall, A.:
748 *geopandas/geopandas: v0.12.1*, Zenodo [code], <https://doi.org/10.5281/zenodo.7262879>, 2022.
- 749 Keulen, N., Malkki, S. N., and Graham, S.: Automated quantitative mineralogy applied to metamorphic rocks,
750 *Minerals*, 10(1), 47, <https://doi.org/10.3390/min10010047>, 2020.
- 751 Lanari, P., Vidal, O., De Andrade, V., Dubacq, B., Lewin, E., Grosch, E. G., and Schwartz, S.: XMapTools: A
752 MATLAB©-based program for electron microprobe X-ray image processing and geothermobarometry, *Comput.*
753 *Geosci.*, 62, 227-240, <https://doi.org/10.1016/j.cageo.2013.08.010>, 2014.
- 754 Le Maitre, R. W.: Classification and nomenclature, in: *Igneous rocks: a classification and glossary of terms: rec-*
755 *ommendations of the International Union of Geological Sciences Subcommission on the Systematics of Igneous*
756 *Rocks*, edited by: Le Maitre, R. W., Streckeisen, A., Zanettin, B., Le Bas, M. J., Bonin, B., and Bateman, P.,
757 Cambridge University Press, <https://doi.org/10.1017/CBO9780511535581>, 2002.



- 758 Li, C., Wang, D., and Kong, L.: Application of machine learning techniques in mineral classification for scanning
759 electron microscopy-energy dispersive X-ray spectroscopy (SEM-EDS) images, *J. Pet. Sci. Eng.*, 200, 108178,
760 <https://doi.org/10.1016/j.petrol.2020.108178>, 2021.
- 761 Li, L., Lee, P. K. K., Tsui, Y., Tham, L. G., and Tang, C. A.: Failure process of granite, *Int. J. Geomech.*, 3(1), 84-
762 98, [https://doi.org/10.1061/\(ASCE\)1532-3641\(2003\)3:1\(84\)](https://doi.org/10.1061/(ASCE)1532-3641(2003)3:1(84)), 2003.
- 763 Mahabadi, O. K., Randall, N. X., Zong, Z., and Grasselli, G.: A novel approach for micro-scale characterization
764 and modeling of geomaterials incorporating actual material heterogeneity, *Geophys. Res. Lett.*, 39(1), [https://](https://doi.org/10.1029/2011gl050411)
765 doi.org/10.1029/2011gl050411, 2012.
- 766 Malac, M., Calzada, J. A. M., Salomons, M., Homeniuk, D., Price, P., Cloutier, M., ... and Egerton, R.: NanoMi:
767 An open source electron microscope hardware and software platform, *Micron*, 163, 103362, [https://doi.org/](https://doi.org/10.1016/j.micron.2022.103362)
768 [10.1016/j.micron.2022.103362](https://doi.org/10.1016/j.micron.2022.103362), 2022.
- 769 Marra, W. A., van de Grint, L., Alberti, K., and Karssenber, D. : Using GIS in an Earth Sciences field course for
770 quantitative exploration, data management and digital mapping, *J. Geogr. Higher Educ.*, 41(2), 213-229, [https://](https://doi.org/10.1080/03098265.2017.1291587)
771 doi.org/10.1080/03098265.2017.1291587, 2017.
- 772 Maxwell, A. E., Warner, T. A., and Fang, F.: Implementation of machine-learning classification in remote sensing:
773 An applied review, *Int. J. Remote Sens.*, 39(9), 2784-2817, <https://doi.org/10.1080/01431161.2018.1433343>,
774 2018.
- 775 McInerney, D., and Kempeneers, P.: Virtual Rasters and Raster Calculations. in: *Open Source Geospatial Tools:*
776 *Applications in Earth Observation, Earth Systems Data and Models.* Springer, [https://doi.org/10.1007/978-3-319-](https://doi.org/10.1007/978-3-319-01824-9_11)
777 [01824-9_11](https://doi.org/10.1007/978-3-319-01824-9_11), 2015.
- 778 Murphy, S. F., Brantley, S. L., Blum, A. E., White, A. F., and Dong, H.: Chemical weathering in a tropical water-
779 shed, Luquillo Mountains, Puerto Rico: II. Rate and mechanism of biotite weathering, *Geochim. Cosmochim.*
780 *Acta*, 62(2), 227-243, [https://doi.org/10.1016/s0016-7037\(97\)00336-0](https://doi.org/10.1016/s0016-7037(97)00336-0), 1998.
- 781 Newbury, D. E., and Ritchie, N. W.: Elemental mapping of microstructures by scanning electron microscopy-en-
782 ergy dispersive X-ray spectrometry (SEM-EDS): extraordinary advances with the silicon drift detector (SDD), *J.*
783 *Anal. At. Spectrom.*, 28(7), 973-988, <https://doi.org/10.1039/c3ja50026h>, 2013.
- 784 Nikonow, W., and Rammlmair, D.: Automated mineralogy based on micro-energy-dispersive X-ray fluorescence
785 microscopy (μ -EDXRF) applied to plutonic rock thin sections in comparison to a mineral liberation analyzer,
786 *Geosci. Instrum. Methods Data Syst.*, 6(2), 429-437, <https://doi.org/10.5194/gi-6-429-2017>, 2017.
- 787 Nikonow, W., Rammlmair, D., Meima, J. A., and Schodlok, M. C.: Advanced mineral characterization and petro-
788 graphic analysis by μ -EDXRF, LIBS, HSI and hyperspectral data merging, *Mineral. Petrol.*, 113, 417-431,
789 <https://doi.org/10.1007/s00710-019-00657-z>, 2019.
- 790 Orlando, J., Comas, X., Hynek, S. A., Buss, H. L., and Brantley, S. L.: Architecture of the deep critical zone in
791 the Río Icacos watershed (Luquillo Critical Zone Observatory, Puerto Rico) inferred from drilling and ground
792 penetrating radar (GPR), *Earth Surf. Processes Landforms*, 41(13), 1826-1840, <https://doi.org/10.1002/esp.3948>,
793 2016.



- 794 Ortolano, G., Visalli, R., Godard, G., and Cirrincione, R.: Quantitative X-ray Map Analyser (Q-XRMA): A new
795 GIS-based statistical approach to Mineral Image Analysis, *Comput. Geosci.*, 115, 56-65, [https://doi.org/10.1016/
796 j.cageo.2018.03.001](https://doi.org/10.1016/j.cageo.2018.03.001), 2018.
- 797 Ortolano, G., Zappalà, L., and Mazzoleni, P.: X-Ray Map Analyser: A new ArcGIS® based tool for the quantita-
798 tive statistical data handling of X-ray maps (Geo-and material-science applications), *Comput. Geosci.*, 72, 49-64,
799 <https://doi.org/10.1016/j.cageo.2014.07.006>, 2014.
- 800 Pedregosa, F., Varoquaux, G., Gramfort, A., Michel, V., Thirion, B., Grisel, O., ... and Duchesnay, É.: Scikit-
801 learn: Machine learning in Python, *J. Mach. Learn. Res.*, 12, 2825-2830, [https://doi.org/10.48550/
802 arxiv.1201.0490](https://doi.org/10.48550/arxiv.1201.0490), 2011.
- 803 Perkins, D.: Mineralogy, Open Educational Resources, University of North Dakota, [https://doi.org/10.31356/
804 oers025](https://doi.org/10.31356/oers025), 2020.
- 805 Pirrie, D., and Rollinson, G. K.: Unlocking the applications of automated mineral analysis, *Geol. Today*, 27(6),
806 226-235, <https://doi.org/10.1111/j.1365-2451.2011.00818.x>, 2011.
- 807 Přikryl, R.: Assessment of rock geomechanical quality by quantitative rock fabric coefficients: limitations and
808 possible source of misinterpretations, *Eng. Geol.*, 87(3-4), 149-162, [https://doi.org/10.1016/
809 j.enggeo.2006.05.011](https://doi.org/10.1016/j.enggeo.2006.05.011), 2006.
- 810 Probst, P., Wright, M. N., and Boulesteix, A. L.: Hyperparameters and tuning strategies for random forest, *Wiley*
811 *Interdiscip. Rev.: Data Min. Knowl. Discovery*, 9(3), e1301, <https://doi.org/10.1002/widm.1301>, 2019.
- 812 Rafiei, M., Löhr, S., Baldermann, A., Webster, R., and Kong, C.: Quantitative petrographic differentiation of de-
813 trital vs diagenetic clay minerals in marine sedimentary sequences: Implications for the rise of biotic soils, *Pre-
814 cambrian Research*, 350, 105948, <https://doi.org/10.1016/j.precamres.2020.105948>, 2020.
- 815 Ramachandran, R., Bugbee, K., and Murphy, K.: From open data to open science, *Earth Space Sci.*, 8(5),
816 e2020EA001562, <https://doi.org/10.1029/2020EA001562>, 2021.
- 817 Raza, A., and Capretz, L. F.: Contributors preference in open source software usability: An empirical study, *arXiv*
818 [preprint], <https://doi.org/10.48550/arXiv.1507.06882>, 24 July 2015.
- 819 Riebe, C. S., Kirchner, J. W., and Finkel, R. C.: Long-term rates of chemical weathering and physical erosion
820 from cosmogenic nuclides and geochemical mass balance, *Geochim. Cosmochim. Acta*, 67(22), 4411-4427,
821 [https://doi.org/10.1016/s0016-7037\(03\)00382-x](https://doi.org/10.1016/s0016-7037(03)00382-x), 2003.
- 822 Reed, M. M., Ferrier, K. L., Nachlas, W. O., Schneider, B., Arson, C., Xu, T., Shen, X., West, N.: Supplement to
823 “A free, open-source method for automated mapping of quantitative mineralogy from energy-dispersive X-ray
824 spectroscopy scans of rock thin sections”, *Zenodo* [code and datasets], <https://doi.org/10.5281/zenodo.10912628>,
825 2024.
- 826 Schulz, B., Sandmann, D., and Gilbricht, S.: SEM-based automated mineralogy and its application in geo-and
827 material sciences, *Minerals*, 10(11), 1004, <https://doi.org/10.3390/min10111004>, 2020.



- 828 Shen, X., Arson, C., Ferrier, K. L., West, N., and Dai, S.: Mineral weathering and bedrock weakening: Modeling
829 microscale bedrock damage under biotite weathering, *J. Geophys. Res.: Earth Surf.*, 124(11), 2623-2646, [https://](https://doi.org/10.1029/2019jf005068)
830 doi.org/10.1029/2019jf005068, 2019.
- 831 Speer, J. A. (1984). Micas in igneous rocks, *Rev. Mineral. Geochem.*, 13(1), 299-356.
- 832 Stallard, R. F., and Murphy, S. F.: Water quality and mass transport in four watersheds in eastern Puerto Rico.
833 Water quality and landscape processes of four watersheds in eastern Puerto Rico. *US Geol. Surv. Prof. Pap.*,
834 1789, 113-152. <https://doi.org/10.3133/pp1789E>, 2012.
- 835 Tapponnier, P., and Brace, W. F.: Development of stress-induced microcracks in Westerly granite. In: *International Journal of Rock Mechanics and Mining Sciences & Geomechanics Abstracts*, [https://doi.org/10.1016/0148-](https://doi.org/10.1016/0148-9062(76)91937-9)
836 [9062\(76\)91937-9](https://doi.org/10.1016/0148-9062(76)91937-9), 1976.
- 838 Tarquini, S., and Favalli, M.: A microscopic information system (MIS) for petrographic analysis, *Comput.*
839 *Geosci.*, 36(5), 665-674, <https://doi.org/10.1016/j.cageo.2009.09.017>, 2010.
- 840 Ündül, Ö.: Assessment of mineralogical and petrographic factors affecting petro-physical properties, strength and
841 cracking processes of volcanic rocks, *Eng. Geol.*, 210, 10-22, <https://doi.org/10.1016/j.enggeo.2016.06.001>,
842 2016.
- 843 Wahrhaftig, C.: Stepped topography of the southern Sierra Nevada, California, *Geol. Soc. Am. Bull.*, 76(10),
844 1165-1190, [https://doi.org/10.1130/0016-7606\(1965\)76\[1165:stotss\]2.0.co;2](https://doi.org/10.1130/0016-7606(1965)76[1165:stotss]2.0.co;2), 1965.
- 845 White, A. F., Blum, A. E., Schulz, M. S., Vivit, D. V., Stonestrom, D. A., Larsen, M., Murphy, S., and Eberl, D.:
846 Chemical weathering in a tropical watershed, Luquillo Mountains, Puerto Rico: I. Long-term versus short-term
847 weathering fluxes, *Geochim. Cosmochim. Acta*, 62(2), 209-226, [https://doi.org/10.1016/s0016-7037\(97\)00335-9](https://doi.org/10.1016/s0016-7037(97)00335-9),
848 1998.
- 849 Xu, T., Shen, X., Reed, M., West, N., Ferrier, K. L., and Arson, C.: Anisotropy and microcrack propagation in-
850 duced by weathering, regional stresses and topographic stresses, *J. Geophys. Res.: Solid Earth*, 127(7),
851 e2022JB024518, <https://doi.org/10.1029/2022JB024518>, 2022.
- 852